Japanese Journal of
Applied Physics

REGULAR PAPER • OPEN ACCESS

Physical masking-induced enhancement of information processing capacity in a redox-type ion-gating reservoir

OPEN ACCESS

Japanese Journal of Applied Physics **64**, 11SP25 (2025) **REGULAR PAPER**

https://doi.org/**10.35848/1347-4065/ae1d84**

Physical masking-induced enhancement of information processing capacity in a redox-type ion-gating reservoir

Daiki Nishioka[1*], Kaoru Shibata[2,3], Wataru Namiki[2], Kazuya Terabe[2], and Takashi Tsuchiya[2,3*]

[1]*International Center for Young Scientists (ICYS), National Institute for Materials Science (NIMS), 1-1 Namiki, Tsukuba, Ibaraki 305-0044, Japan*
[2]*Research Center for Materials Nanoarchitectonics (MANA), National Institute for Materials Science (NIMS), 1-1 Namiki, Tsukuba, Ibaraki 305-0044, Japan*
[3]*Department of Applied Physics, Tokyo University of Science, Katsushika, Tokyo 125-8585, Japan*

[*]E-mail: NISHIOKA.Daiki@nims.go.jp; TSUCHIYA.Takashi@nims.go.jp

Received October 22, 2025; revised October 31, 2025; accepted November 9, 2025; published online November 24, 2025

We analyzed the computational mechanism of redox-type ion-gating reservoirs (Redox-IGRs)—a class of physical reservoir computing (PRC) devices that utilize redox dynamics induced by ion gating for information processing—operated with physical masking (PM), in which a simple triangular drain voltage dynamically modulates the conductance of the device. The periodic drain perturbation enriches the temporal diversity of the conductance response, leading to enhanced nonlinear dynamics. Information-processing-capacity (IPC) analysis revealed that PM markedly increases nonlinear capacity while maintaining linear memory capacity, resulting in a total IPC increase from 11 to 20. This doubling of IPC indicates an expansion of the reservoir's effective dimensionality and explains the improved performance observed in nonlinear dynamical system prediction tasks. These findings demonstrate that PM effectively enhances the expressive power of Redox-IGRs and provides a simple, general strategy for boosting the high-dimensional dynamics of PRC systems. © 2025 The Author(s). Published on behalf of The Japan Society of Applied Physics by IOP Publishing Ltd

Supplementary material for this article is available online

1. Introduction

The remarkable progress of artificial intelligence (AI) in recent years has brought significant benefits to human society,[1)] yet it has also raised the critical challenge of exponentially increasing power consumption. This issue largely arises from the intrinsic mismatch between conventional von Neumann computing architectures and the nature of information processing in brain-inspired AI models. To overcome this limitation, neuromorphic devices that directly emulate brain-like computation are attracting increasing attention.[2)] The excessive power demand of conventional computing is problematic not only in terms of sustainability but also because it hinders the deployment of high-performance AI functions in resource-constrained edge environments.[3)] Accordingly, the realization of energy-efficient neuromorphic computing systems is urgently required, particularly for edge applications. Among various approaches to neuromorphic computing, physical reservoir computing (PRC) has emerged as a promising candidate.[4,5)] In contrast to device-level implementations of hierarchical neural networks in in-memory computing, PRC ambitiously replaces neurons and synapses in a randomly connected recurrent network layer —the reservoir[6,7)]—with one or a few physical systems. By exploiting the inherent nonlinearity, short-term memory, and high dimensionality of the physical reservoir, input signals can be mapped into a high-dimensional space, where classification and regression tasks are performed using a small linear readout layer. Because the majority of computation is offloaded to the physical processes of the reservoir and the learnable readout is linear, PRC offers substantial reductions in computational cost. Various physical systems have been explored as reservoirs, including spin-torque oscillators, spin waves, memristors, nanowire networks, soft bodies, photonic circuits, and so on.[4,5,8–35)] These systems have demonstrated the feasibility of PRC for a wide range of information processing tasks such as time-series prediction, image recognition, and anomaly detection. However, achieving both high computational performance and small device footprints—essential for integration and edge applications—remains a formidable challenge.

To address this limitation, we have recently developed ion-gating reservoirs (IGRs) as a framework to fully exploit the intrinsic information processing capability of ion-conducting materials.[36–47)] An IGR consists of electrodes for voltage input, ion conductors that drives ionic carriers, and functional channel materials that exhibit nonlinear responses under ion gating. Depending on the choice of channel material, diverse physical processes—such as electrostatic modulation of electronic properties in ion-gated transistors, ionic control of spin-wave propagation in ferromagnetic materials, or ionically induced modulation of molecular vibration dynamics—can serve as computational resources for PRC. Notably, the electric double layer IGR (EDL-IGR), composed of a hydrogen-terminated diamond channel and a Li–Sr–Zr–O solid electrolyte, has successfully demonstrated the coexistence of high computational performance and compact device size in the standard nonlinear autoregressive moving-average (NARMA2) benchmark task.[36)] For edge AI applications, however, high performance and small size are not sufficient: the temporal scale of the reservoir dynamics must also match the timescale of the target signals. For example, in sensor-processor integrated edge devices, slow dynamics such as biosignals or long-period seismic waves require reservoirs that can operate efficiently below 1 Hz. Although EDL-IGRs exhibit relatively fast dynamics dominated by EDL effects, their operational frequency range is typically limited to above 10 Hz, making them unsuitable for such slow signals.[36,42,47)] Redox-based IGRs, in which the channels are ion–electron mixed conductors, can operate at

lower frequencies, but their computational performance is significantly inferior to that of EDL-IGRs.[37,46)] This limitation stems from the fact that redox dynamics generally yield simple relaxation-type responses, whereas EDL systems exhibit complex pseudo-synaptic dynamics arising from coupled ion–electron interactions.

In this study, we overcome this challenge by introducing a physical masking (PM) strategy into $LiCoO_2$ channel-based Redox-IGRs.[38)] Specifically, the drain voltage used to probe the channel current (reservoir state) is replaced from a constant bias to a periodic triangular waveform. This maintains the device in a transient regime and induces more complex responses. Unlike conventional digital masking,[48)] which requires preprocessing of the input signals by multiplication with mask matrices, PM requires no such preprocessing and is therefore advantageous for edge implementation. While the basic concept of PM was previously reported at the 2025 International Conference on Solid State Devices and Materials (SSDM 2025),[49)] the present study further demonstrates that combining PM with the inverted input method leads to a substantial improvement in computational performance. We evaluate the impact of PM on the information processing capacity (IPC) of Redox-IGRs—a task-independent metric that quantitatively assesses nonlinearity, memory, and dimensionality—and reveal the origin of the performance enhancement.[50,51)] Furthermore, we demonstrate that combining PM with inversion pulse input method substantially improves computational performance. To quantitatively evaluate this improvement, we employed the second-order NARMA2 task—a standard benchmark task in PRC that assesses the ability of a reservoir to predict the behavior of nonlinear dynamical systems. In the NARMA2 task, our redox-IGR without PM exhibits a normalized mean squared error (NMSE) of 0.21, whereas applying PM reduces the NMSE to 0.033 at an operational frequency of 50 mHz, representing state-of-the-art performance among PRC systems operating below 1 Hz.[33,34,37,43,46,52,53)] In addition, the total IPC increases from 11 (without PM) to 20 (with PM), primarily due to enhanced nonlinear capacity, indicating that PM effectively doubles the dimensionality of the system. These results establish PM as a powerful strategy for extending the computational performance of PRC into previously inaccessible low-frequency regimes, opening pathways for edge-AI devices capable of processing slow temporal dynamics.

2. Method

A schematic illustration of the $LiCoO_2$ Redox-IGR used in this study is shown in Fig. 1(a). Ti (5 nm)/Pt (35 nm) source and drain electrodes were deposited by electron-beam evaporation on $SrTiO_3$ (100) substrates. A (104)-oriented $LiCoO_2$ (LCO) channel layer with a thickness of approximately 100 nm was deposited by pulsed laser deposition using a 266 nm Nd:YAG laser under an oxygen atmosphere, with the substrate temperature maintained at 600 °C. As the solid electrolyte, an amorphous Li_3PO_4 film (~300 nm) was deposited by RF sputtering in Ar atmosphere. A Si layer (~20 nm) was deposited as the gate electrode, followed by a Pt current collector (50 nm) by electron-beam evaporation. The device geometry consisted of one source and two drain electrodes, defining channel lengths of 5 and 20 μm, and a channel width of 500 μm. Further details of the fabrication process are described in our previous report.[38)] Electrical characterization of the devices and measurements for information processing tasks were performed using a semiconductor parameter analyzer (4200A-SCS, Keithley) equipped with source–measure units. During the measurements, the devices were placed in a vacuum chamber evacuated by a turbomolecular pump and maintained at room temperature. Electrical contact was made using tungsten probes. Gate voltages (V_G) were applied to drive ionic motion within the solid electrolyte, while the drain currents (I_D) were monitored to obtain the reservoir states. In experiments with PM, the drain voltage (V_D) was supplied as a periodic triangular waveform, whereas control measurements were performed under a constant drain bias.

3. Results

3.1. Concept of physical masking

The Redox-IGR used in this study has a multi-terminal transistor structure composed of two drain terminals, one common gate, and one common source, as schematically shown in Fig. 1(a). The input information is applied as a sequence of pulsed gate voltages. Upon application of these inputs, lithium-ion transport within the solid electrolyte and subsequent insertion and extraction of lithium ions into and from the LCO channel occur, leading to redox reactions that modulate both the hole concentration and hole mobility of the channel.[54)] The resulting conductance variations of the LCO channel are monitored as the drain current, which serves as the reservoir states representing the nonlinear responses of the system to the input signals. In conventional IGR operation, the drain current is measured under a constant drain bias, as in standard ion-gated transistors [Fig. 1(b)].[37,55)] This configuration corresponds to the case without PM. When the internal device dynamics are sufficiently complex—such as in EDL-IGRs composed of hydrogen-terminated diamond channels and Li^+ solid electrolytes—the coupled ion–electron dynamics at the electrolyte/channel interface can exhibit edge-of-chaos behavior, resulting in high computational performance.[36)] However, in typical redox-type transistors composed of oxide channels such as WO_3 and Li^+ solid electrolytes, the conductance modulation follows relatively simple relaxation dynamics limited by ion diffusion within the ion–electron mixed conductor channel. This diffusive and monotonic behavior is the primary reason for the lower computational performance observed in conventional redox-IGRs.[37)] To overcome this limitation, we introduce PM, in which the drain current is measured under a periodically varying triangular drain voltage, as illustrated in Fig. 1(c). In this configuration, not only the gate input but also the dynamic variation of the drain voltage contributes to the effective ion gating, thereby maintaining the system in a transient, non-equilibrium state and enhancing the complexity of its response. As described later in detail, the use of triangular drain voltages with different amplitudes and frequencies, as shown in Fig. 1(c), allows the PM conditions to coexist in each channel with distinct transient behaviors, which is expected to enhance the overall high dimensionality of the device. Unlike conventional digital masking, which applies a random or binary mask matrix to the input sequence as a preprocessing

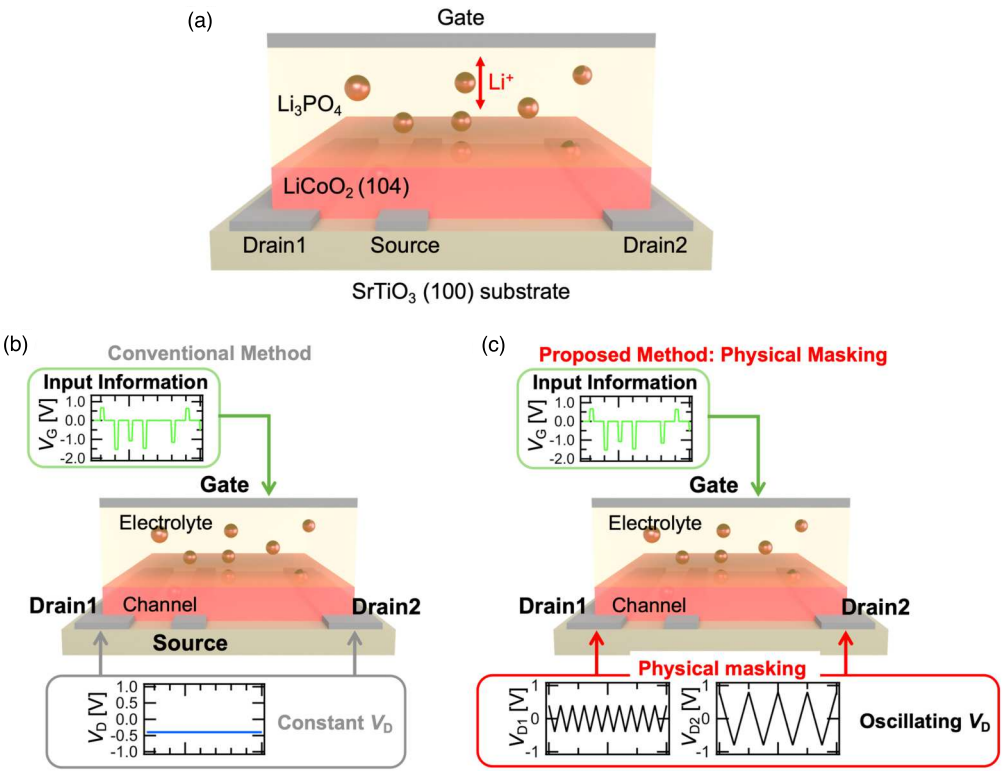

Fig. 1. (a) Schematic illustration of the redox-type ion-gating reservoir used in this study. (b) Conventional operation scheme, in which input information is applied as a pulsed gate-voltage sequence and the drain currents are measured under a constant drain voltage. (c) Device operation with physical masking, where a periodic triangular drain-voltage waveform is applied instead of a constant bias for current measurement.

step,[24,25,48] PM requires no such external signal processing and is thus advantageous for hardware implementation in edge environments. Furthermore, because PM manipulates the intrinsic dynamics of the device itself rather than the input data, this concept can be broadly applied to various types of physical reservoir systems that can accept multiple input channels, beyond the scope of IGRs.

3.2. Effect of physical masking on conductance modulation dynamics

Figure 2 illustrates the effect of PM on the temporal evolution of conductance modulation in the Redox-IGR. When a sequence of pulsed gate voltages, shown in the upper panels of Figs. 2(a) and 2(b), is applied to the gate, the drain current is measured either under a constant drain bias [Fig. 2(a), middle] or under a triangular drain voltage (with PM) [Fig. 2(b), middle]. The channel conductance ($G = I_D/V_D$) calculated from these measurements exhibits markedly different behaviors depending on the drain-bias condition. In the absence of PM, as shown in the lower panel of Fig. 2(a), the conductance responds to the gate-voltage pulses in a simple relaxation manner, reflecting the slow redox dynamics of lithium-ion diffusion and insertion/extraction within the LCO channel.[54] Such monotonic relaxation responses lead to high correlation between adjacent temporal states in the virtual-node (time-multiplexing) representation commonly used in reservoir computing.[48] Consequently, the effective reservoir dimensionality—i.e. the number of functionally independent virtual nodes—becomes significantly smaller than the nominal number of sampled nodes. (Details of the virtual-node approach in IGR systems are discussed elsewhere.[36,37]) By contrast, when a simple triangular drain voltage is applied during measurement [Fig. 2(b)], the conductance response shows far more diverse and intricate temporal behavior, as seen in the lower panel. This enhanced complexity mitigates the aforementioned redundancy among adjacent virtual nodes, thereby increasing the effective dimensionality of the reservoir state space.

The origin of this behavior can be explained in terms of the effective gate voltage, ($V_{G,eff} = V_G - V_D/2$), acting on the channel. As depicted in Fig. 2(c), under a constant V_D, $V_{G,eff}$ varies solely with the externally applied gate voltage. Hence, for a given input pulse of V_G, the conductance G simply relaxes toward its steady-state value on the master (G–V_G) curve [inset of Fig. 2(c)], with a time constant determined by the ionic resistance of the electrolyte, the chemical capacitance and the electronic resistance of the channel. In contrast, when a triangular V_D is applied [Fig. 2(d)], $V_{G,eff}$ continuously oscillates with V_D, resulting in dynamic modulation of G even at a fixed gate-input level. Consequently, G is no longer uniquely defined for each V_G; instead, it fluctuates within a finite range that reflects the instantaneous V_D variation. However, as shown in the lower panel of Fig. 2(b), the amplitude of this fluctuation is smaller than that induced directly by the gate voltage. Considering the relation $G \propto \sigma = \mu pe$, (where σ is the electrical conductivity, μ is the hole mobility, p is the hole carrier density, and e is the elementary charge), it can be inferred that during such small fluctuations, the mobility μ remains almost constant, and the variation in G mainly corresponds to a change in the carrier density p. Since p in this device reflects the amount of Li inserted into the LCO channel, it is considered that, under PM operation, Li^+ are inserted into or extracted from the channel in response to the applied V_G, while Li^+ near the channel/electrolyte interface are further driven by the oscillating V_D,

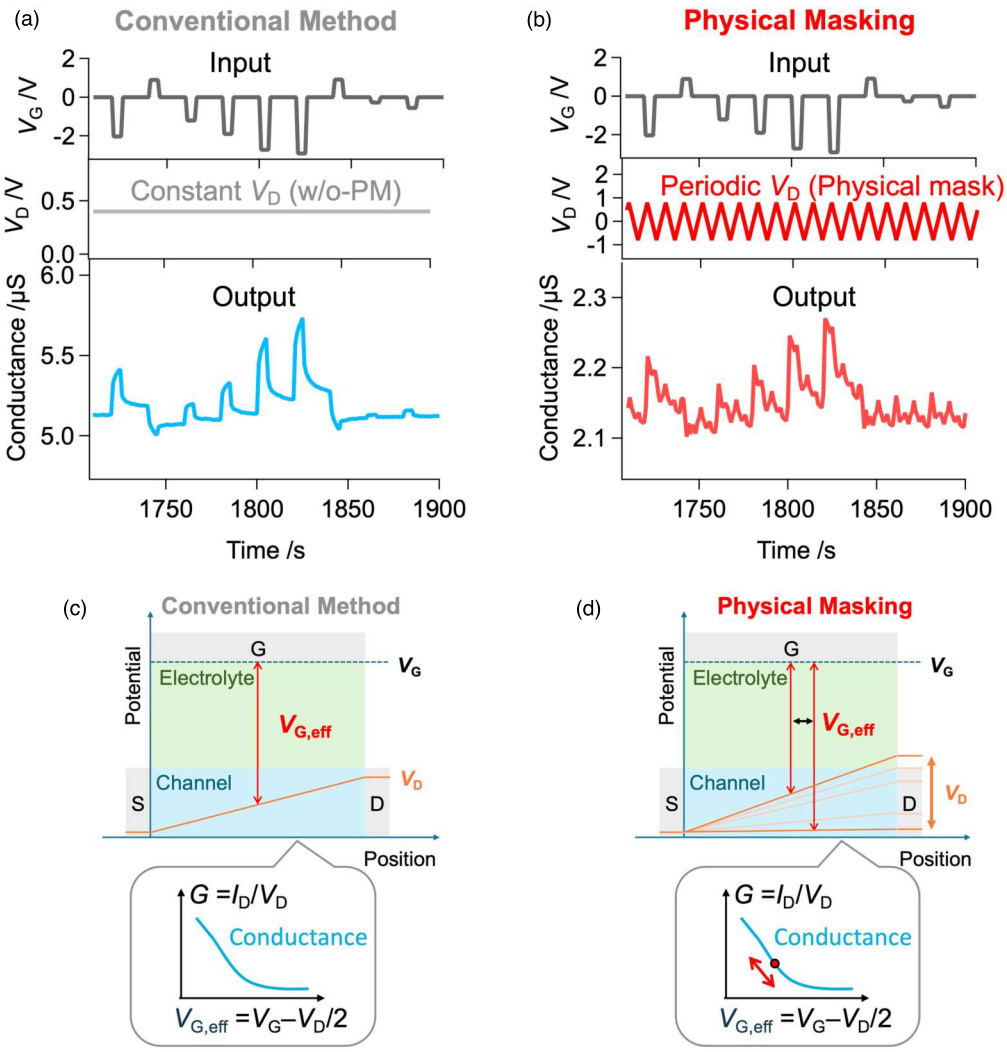

Fig. 2. Input–output characteristics of the device (a) without and (b) with physical masking. Each panel shows the input gate-voltage sequence (top), the drain voltage (middle), and the corresponding conductance response (bottom). Schematic illustrations of the effective gate voltage for (c) operation without PM and (d) operation with PM.

repeatedly undergoing insertion and extraction synchronized with V_D. This analysis suggests that such interfacial Li^+ motion contributes to the complex conductance modulation observed under PM operation. As illustrated in the inset of Fig. 2(d), this corresponds to sampling a broader portion of the nonlinear (G–$V_{G,eff}$) characteristic, effectively activating a richer set of nonlinear responses intrinsic to the device. These results indicate that PM enables the Redox-IGR to more efficiently utilize its inherent nonlinearity for information processing by maintaining the system in a dynamically perturbed state.

3.3. Performance evaluation using a second-order nonlinear dynamical system task

To evaluate the effect of the triangular-wave drain voltage-based PM on the computational performance of the Redox-IGR, we employed the NARMA2 task, which is widely used for assessing reservoir computing systems.[27,29,33,34,36,37,47,56] The NARMA2 system is defined as

$$y_{tar}(k+1) = 0.4y_{tar}(k) + 0.4y_{tar}(k)y_{tar}(k-1) + 0.6u^3(k) + 0.1, \quad (1)$$

where $u(k)$ is a random input uniformly distributed between 0 and 0.5, and k denotes discrete time. The objective of this task is to train the reservoir to reproduce the system output $y_{tar}(k)$ from the given input sequence $u(k)$. Accurate prediction requires that the reservoir possesses nonlinear and memory characteristics comparable to those inherent in the NARMA2 system.

Figure 3(a) schematically illustrates the information-processing scheme used in the present work. The input signal $u(k)$ was converted into a pulsed-voltage sequence (base voltage = 0 V, maximum = +1 V, minimum = −3 V) with a frequency of 50 mHz and a duty cycle of 25%, and applied to the gate terminal of the device. During operation, two drain terminals were driven by triangular-wave voltages serving as physical masks: one with an amplitude of ±0.4 V at 250 mHz and the other with ±0.8 V at 100 mHz. For comparison, control experiments without PM were performed by applying constant drain biases of 0.4 V to both terminals. The effect of these PM conditions on the prediction error in the NARMA2 task and on the information-processing capacity (IPC) is summarized in supplementary Fig. 1, and the details of the IPC analysis are described in a later section. Although larger amplitudes and higher frequencies of the triangular drain voltages tend to improve the computational performance of the IGR, the best performance was achieved when different voltages and frequencies were applied simultaneously to the two drain terminals.

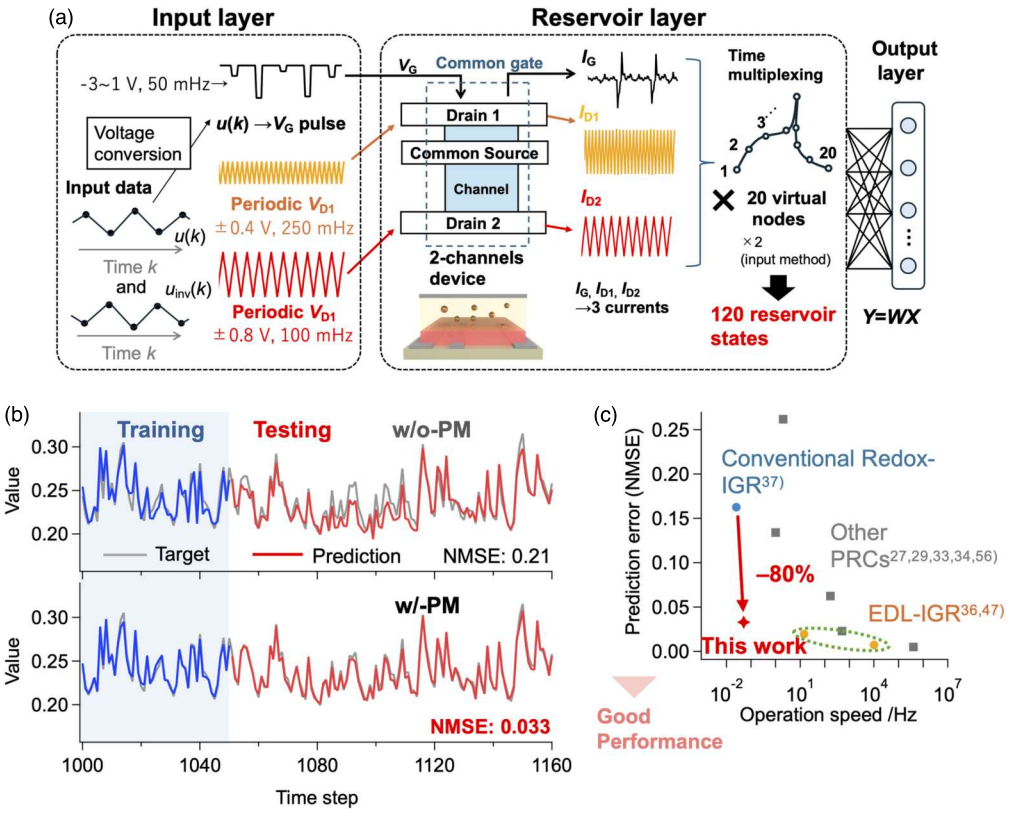

Fig. 3. (a) Schematic illustration of the information-processing scheme in the Redox-IGR. The input information was converted into a pulsed sequence at 50 mHz and applied as the gate voltage. From the three measured current responses, 20 virtual nodes were extracted. The same procedure was performed for the inverted input, yielding 120 reservoir states in total. The reservoir output was computed as a linear combination of these states and the trained readout weights. (b) Results of the NARMA2 task for operation (top) without and (bottom) with physical masking (PM). Gray lines represent the target sequence, while blue and red lines denote the reservoir-predicted waveforms during training and testing, respectively. (c) Comparison of the prediction error for the NARMA2 test data as a function of the device operating frequency with other PRC systems.[27,29,33,34,36,37,47,56)]

Based on these observations, the PM conditions described above were adopted throughout this study. For each input sequence, the gate current (I_G) and two drain currents were recorded as physical nodes, and twenty current values were sampled per input period (five points during the "pulse-on" phase and fifteen during the interval) at a sampling rate of 1 Hz to generate virtual nodes at equal time intervals. Combining the three current responses and the twenty virtual nodes yielded a total of 60 reservoir states. An example of the current response and the corresponding sampling points for the virtual nodes is shown in supplementary Fig. 2. As noted above, the two triangular drain voltages have frequencies different from that of the gate input; however, as shown in supplementary Fig. 2, all signals operate in the same phase at each discrete time step. To ensure consistency among the virtual nodes, the frequencies of the PM signals were selected under this condition. To further enhance the computational performance, the inversion input method was also employed: an inverted signal ($u_{\mathrm{inv}}(k) = u_{\max} - u(k)$, ($u_{\max} = 0.5$)) was created, and reservoir states were generated following the same procedure. Details of this inversion method are described elsewhere.[40)] Consequently, a 120-dimensional reservoir state vector ($x_1(k)$, $x_2(k)$, …, $x_{120}(k)$) was obtained for each input $u(k)$, and the reservoir output was calculated as a linear combination of the states and readout weights:

$$Y = WX, \tag{2}$$

where $Y = (y(1), y(2), \ldots)$ denotes the reservoir output vector, $X = (\boldsymbol{x}(1), \boldsymbol{x}(2), \ldots)$ is the reservoir-state matrix, $\boldsymbol{x}(k) = (1, x_1(k), x_2(k), \ldots, x_{120}(k))^{\mathrm{T}}$ is the reservoir state vector, and $W = (w_0, w_1, \ldots, w_{120})$ is the readout-weight vector. The readout weights were trained by ridge regression ($W = Y_{\mathrm{tar}}X^{\mathrm{T}}(XX^{\mathrm{T}} + \lambda I)^{-1}$, where $Y_{\mathrm{tar}} = (y_{\mathrm{tar}}(1), y_{\mathrm{tar}}(2), \ldots)$ is the target vector, I is the identity matrix) with a regularization parameter ($\lambda = 5 \times 10^{-4}$), using 50 data for washout, 1000 data for training, and 200 data for testing. The computational performance was evaluated using the NMSE defined as;

$$\mathrm{NMSE} = \frac{1}{L}\frac{\sum_{k=1}^{L}[y_{\mathrm{tar}}(k) - y(k)]^2}{\mathrm{var}[y_{\mathrm{tar}}(k)]}, \tag{3}$$

where var(·) denotes the variance, and L represents the data length (1000 for training and 200 for testing).

Figure 3(b) compares the target and reservoir outputs for the cases without PM (top) and with PM (bottom). Without PM, the reservoir output shows limited agreement with the target, yielding NMSEs of 0.081 for training and 0.21 for testing. When PM was applied, the reservoir output closely matched the target, and the NMSEs decreased to 0.021 (training) and 0.033 (testing), corresponding to an 85% reduction in test error. These results clearly demonstrate that PM significantly enhances the computational capability of the Redox-IGR. Supplementary Table 1 summarizes the NMSEs obtained under PM operation using six-fold cross-

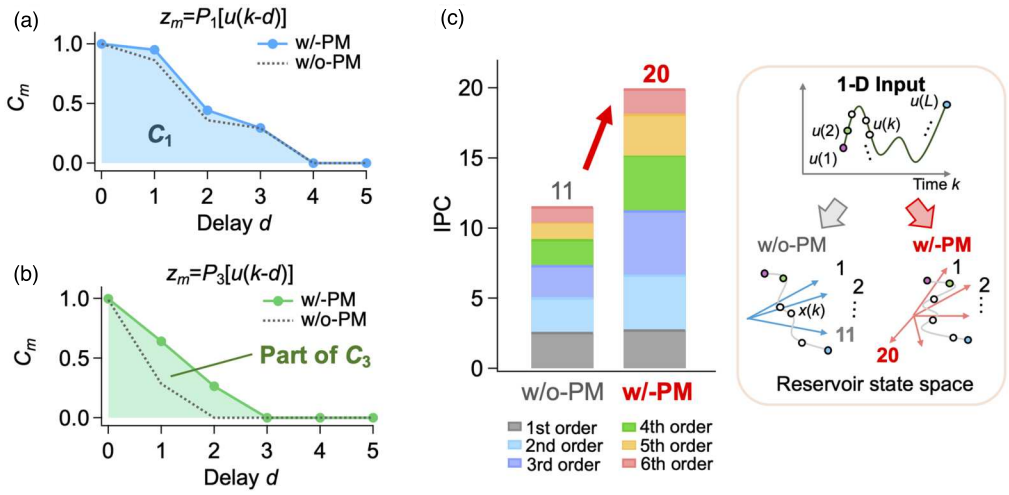

Fig. 4. (a) Relationship between the component-wise capacity C_m and delay for targets representing linear nonlinearity. Cyan plots and gray dashed lines indicate the results with and without PM, respectively. (b) Relationship between C_m and delay for targets representing cubic nonlinearity. Green plots and gray dashed lines indicate the results with and without PM, respectively. (c) Total capacity of the Redox-IGR, color-coded by degree-specific capacity. The total capacity nearly doubles with the application of PM. Because the total capacity reflects the effective dimensionality of the reservoir-state matrix, the inset schematically illustrates how the IGR maps one-dimensional input information into a higher-dimensional space.

validation (with 1000 steps for training and 200 steps for testing; the schematic procedure is illustrated in supplementary Fig. 3). The NMSEs for the test datasets ranged from 0.027 to 0.044, with an average of 0.034, indicating consistent and robust performance regardless of the specific training or testing dataset used. Figure 3(c) summarizes the relationship between the test error and operational frequency for various PRC systems. The PM-enhanced Redox-IGR successfully overcomes the inherent low-performance limitation of conventional redox-type reservoirs and achieves state-of-the-art accuracy in the sub-1 Hz regime. While high-performance PRCs—such as EDL-IGRs, spin-wave reservoirs, and photonic circuits—are typically realized in high-frequency domains,[14,24–27,36,45,47,56] few systems have exhibited comparable performance at such low operation speeds. Thus, the PM-driven Redox-IGR represents a promising class of low-frequency, high-performance physical reservoirs, capable of processing slow dynamical signals such as low-frequency components of biological rhythms (heartbeat, respiration, glucose variation) or long-period seismic waves, thereby paving the way for future edge-AI processors optimized for slow temporal dynamics.

3.4. Information-processing-capacity analysis

To elucidate the origin of the performance enhancement in the PM-assisted IGR, we evaluated the IPC of the device. The IPC provides a quantitative measure of a reservoir's computational ability, directly characterizing its memory and nonlinear transformation capabilities.[50,51] In this analysis, a random input sequence $u(k)$ taking values between –1 and 1 was applied to the reservoir, and the accuracy with which the reservoir reconstructed a set of orthogonal-polynomial target functions $z_m(k)$—generated from delayed versions of the input—was used to compute the capacities. The target functions were defined as

$$z_m(k) = \prod_{d=0}^{D} P_{n_{m,d}}[u(k-d)], \tag{4}$$

where m is the target index, d is the delay step, D is the maximum delay, and $n_{m,d}$ denotes the polynomial order corresponding to each combination of m and d.

Here, $P_{n'}$ represents a set of orthogonal polynomials constructed via Gram–Schmidt orthogonalization as

$$P_{n'}[u(k-d)] = u^{n'}(k-d) - \sum_{i=0}^{n'-1} c_i^{(n')} P_i[u(k-d)] \tag{5}$$

$$c_i^{(n')} = \frac{\sum_{k=1}^{T} P_i[u(k-d)]u^{n'}(k)}{\sum_{k=1}^{T} P_i[u(k-d)]^2} \tag{6}$$

with $P_0 = 1$. Thus, the degree of nonlinearity for each target z_m is defined as $n = \sum_{d=0}^{D} n_{m,d}$. The component-wise capacity (C_m), which represents the reservoir's ability to reconstruct the target z_m, was calculated from the reconstruction accuracy as

$$C_m = 1 - \frac{\sum_k [z_m(k) - y(k)]^2}{\sum_k [z_m(k)]^2} \tag{7}$$

and the total capacity was defined as the sum of all partial capacities:

$$C_{\text{tot}} = \sum_m C_m. \tag{8}$$

To avoid overestimation of the IPC, a surrogate analysis was applied: the time order of each target sequence z_m was randomly shuffled to obtain the surrogate capacity C_{sur}, and any C_m values below 1.5 times the maximum of C_{sur} were set to zero. This surrogate procedure serves as a safeguard against spurious capacity contributions, as discussed elsewhere.[11] The degree-specific capacity C_n, which characterizes a specific degree of nonlinearity, is defined as follows.

$$C_n = \sum_{m(n)} C_m. \tag{9}$$

Here, $m(n)$ represents all indices of total degree n. By examining the capacities corresponding to each nonlinear component, one can directly assess how effectively the reservoir performs nonlinear transformations of different degrees.

For instance, when $n = 1$, ($z_m = P_1[u(k-d)] = u(k-d) - \bar{u}$); the corresponding capacity C_1 represents the linear (memory) capacity that quantifies how accurately the reservoir can recall past inputs. Figure 4(a) shows the delay-length dependence of the component-wise capacities for the cases with and without PM. As the delay increases, the C_m decreases, indicating the decay of memory over time—the so-called forgetting curve. The integral of this curve corresponds to the linear capacity C_1, which was found to be similar for both cases, suggesting that PM has little effect on the short-term memory of the device. In contrast, Fig. 4(b) presents the case for third-order nonlinear targets ($z_m = P_3[u(k-d)]$), where the reservoir must reconstruct cubic transformations of past inputs. Here, the PM-assisted IGR exhibits significantly higher capacities than the non-PM device, indicating improved nonlinear processing capability. The total third-order capacity C_3 was obtained by summing all relevant partial capacities, including cross-terms such as $P_1[u(k-d_1)]P_2[u(k-d_2)]$, $(d_1 \neq d_2)$ and $P_1[u(k-d_1)]P_1[u(k-d_2)]P_1[u(k-d_3)]$, $(d_1 < d_2 < d_3)$.

The overall distribution of capacities across specific degree of nonlinearity is summarized in Fig. 4(c). While the linear capacity C_1 shows minimal difference between the two conditions, the nonlinear capacities $C_{n\geqslant 2}$ of second order and higher increase markedly with PM. This finding reveals that the improved performance in the NARMA2 task originates from enhanced nonlinear processing rather than from improved linear memory capacity. Specifically, the total capacity C_{tot} increased from 11 without PM to 20 with PM—nearly a twofold enhancement. Since the total IPC is mathematically equivalent to the rank of the reservoir-state matrix ($C_{\mathrm{tot}} = \mathrm{rank}(X)$),[50] this result implies that the effective dimensionality of the reservoir expanded from 11 to 20 with PM. As schematically illustrated in the inset of Fig. 4(c), the non-PM IGR maps a one-dimensional input into an 11-dimensional effective state space, whereas the PM-assisted IGR expands this mapping into a 20-dimensional space. The dimensional enhancement arises mainly from increased diversity among virtual nodes. As discussed in Sect. 3.2, without PM the neighboring virtual nodes tend to exhibit similar temporal behaviors due to the simple relaxation dynamics of the channel, resulting in a substantial reduction in effective dimensionality. In contrast, PM continuously perturbs the effective gate voltage and suppresses such redundancy, thereby enriching the reservoir state space. These results demonstrate that PM is a simple yet powerful approach to enhance both the high-dimensionality and nonlinearity of physical reservoirs. Moreover, because PM operates by modulating intrinsic device dynamics rather than external signal preprocessing, it can be broadly applied to various PRC systems that accept multi-input excitation, such as nanowire networks, chemical reactions, transistors, beyond the IGR architecture.[16,17,21,23,27,29,31,32,52] In particular, recent theoretical studies on spin-wave-based reservoirs and memristor network reservoirs have reported that increasing the number of detection terminals enhances the system's dimensionality, thereby improving computational performance.[57–59] Accordingly, introducing PM into such multi-input systems is expected to further expand their dimensionality and consequently enhance their computational capability. Since PM is implemented by applying a periodic voltage signal to the physical system, it can be realized with minimal additional circuitry and without any preprocessing of the input signals, which is a significant advantage for practical device operation. In future work, the performance of PM-enhanced IGRs—including both redox-type and EDL-type IGRs—will be further investigated in more complex and practical tasks, such as biological signal processing and environmental sensing, where temporal features are highly nonstationary and information extraction is particularly challenging. Such studies will pave the way toward the realization of edge-AI systems that directly integrate sensing and computation within a single IGR-based platform, enabling energy-efficient processing of real-world temporal data.

4. Conclusion

In this study, we demonstrated that introducing a PM scheme —implemented as a triangular-wave drain voltage—significantly enhances the computational performance of redox-type IGRs. The PM effectively maintains the device in a dynamically perturbed state, thereby enriching the temporal diversity of the conductance response. This leads to an expansion of the reservoir's effective dimensionality and a pronounced improvement in nonlinear information processing capability. Computing performance evaluation using the NARMA2 task revealed that PM reduces the prediction error by 85% compared with the conventional constant-bias configuration, achieving state-of-the-art performance among PRC systems operating below 1 Hz. IPC analysis further clarified that the improvement arises primarily from enhanced nonlinear capacity rather than increased memory capacity, with the total IPC doubling from 11 to 20 under PM operation. This corresponds to a substantial increase in the effective rank of the reservoir-state space, confirming that PM provides a simple yet powerful means to expand the computational dimensionality of physical reservoirs. The PM-based approach requires no additional preprocessing of input signals and is therefore highly suitable for hardware implementation in edge environments. Moreover, since the concept relies solely on the dynamic modulation of device operation, it can be universally extended to other physical reservoir systems that accept multiple inputs, including spintronic, photonic, and electrochemical platforms.[60–70] These findings establish PM as a general and energy-efficient strategy for enhancing the high-dimensional nonlinear dynamics of physical reservoirs, and pave the way toward next-generation low-frequency, high-performance edge-AI processors capable of handling slow temporal signals such as biological rhythms and geophysical data.

Acknowledgments

This research was in part supported by JST PRESTO Grant Nos. JPMJPR23H4 and JSPS KAKENHI Grant Nos. JP24KJ0299 (Grant-in-Aid for JSPS Fellows) and JP25K17941. A part of this work was supported by "Advanced Research Infrastructure for Materials and Nanotechnology in Japan (ARIM)" of the Ministry of Education, Culture, Sports, Science and Technology (MEXT).

Proposal Number JPMXP1224NM5236 and JPMXP1225NM 5329. Daiki Nishioka acknowledges the International Center for Young Scientists (ICYS) at NIMS for providing ICYS fellowships.

ORCID iDs

Daiki Nishioka https://orcid.org/0000-0002-3369-7700
Wataru Namiki https://orcid.org/0000-0003-4053-7366
Kazuya Terabe https://orcid.org/0000-0003-3988-3456
Takashi Tsuchiya https://orcid.org/0000-0002-6950-6160

1) Y. LeCun, Y. Bengio, and G. Hinton, Nature **521**, 436 (2015).
2) D. V. Christensen et al., Neuromorphic Comput. Eng. **2**, 022501 (2022).
3) W. Shi, J. Cao, Q. Zhang, Y. Li, and L. Xu, IEEE Internet Things J. **3**, 637 (2016).
4) G. Tanaka, T. Yamane, J. B. Héroux, R. Nakane, N. Kanazawa, S. Takeda, H. Numata, D. Nakano, and A. Hirose, Neural Netw. **115**, 100 (2019).
5) K. Nakajima, Jpn. J. Appl. Phys. **59**, 60501 (2020).
6) H. Jaeger, German Nat. Res. Center Inf. Technol., GMD Tech. Rep. **148**, 1 (2001).
7) H. Jaeger and H. Haas, Science **304**, 78 (2004).
8) O. Lee et al., Nat. Mater. **23**, 79 (2024).
9) J. Torrejon, M. Riou, F. A. Araujo, S. Tsunegi, G. Khalsa, D. Querlioz, P. Bortolotti, V. Cros, K. Yakushiji, and A. Fukushima, Nature **547**, 428 (2017).
10) R. Nakane, G. Tanaka, and A. Hirose, IEEE Access **6**, 4462 (2018).
11) S. Tsunegi et al., Adv. Intelligent Syst. **5**, 2300175 (2023).
12) N. Akashi, T. Yamaguchi, S. Tsunegi, T. Taniguchi, M. Nishida, R. Sakurai, Y. Wakao, and K. Nakajima, Phys. Rev. Res. **2**, 43303 (2020).
13) S. Tsunegi, T. Taniguchi, K. Nakajima, S. Miwa, K. Yakushiji, A. Fukushima, S. Yuasa, and H. Kubota, Appl. Phys. Lett. **114**, 164101 (2019).
14) W. Namiki, D. Nishioka, Y. Yamaguchi, T. Tsuchiya, T. Higuchi, and K. Terabe, Adv. Intelligent Syst. **5**, 2300228 (2023).
15) C. Du, F. Cai, M. A. Zidan, W. Ma, S. H. Lee, and W. D. Lu, Nat. Commun. **8**, 2204 (2017).
16) K. Toprasertpong, R. Suzuki, S.-Y. Min, E. Nako, R. Nakane, M. Takenaka, and S. Takagi, Jpn. J. Appl. Phys. **64**, 090801 (2025).
17) M. Desu, A. Karacali, Y. Usami, Y. Ishizaki-Betchaku, S. Nagano, M. Xu, S. S. Pandey, and H. Tanaka, Jpn. J. Appl. Phys. **64**, 04SP12 (2025).
18) Y. Ohno, H. Tanaka, and T. Hasegawa, Jpn. J. Appl. Phys. **64**, 03SP15 (2025).
19) S. Ohara, K. Kanno, A. Uchida, and H. Kurokawa, Jpn. J. Appl. Phys. **64**, 012001 (2025).
20) N. Hosoda, H. Komatsu, and T. Ikuno, Jpn. J. Appl. Phys. **64**, 017001 (2025).
21) R. Suzuki, K. Toprasertpong, R. Nakane, E. Nako, M. Takenaka, and S. Takagi, Jpn. J. Appl. Phys. **64**, 02SP40 (2025).
22) R. Yamada, M. Nakagawa, S. Hirooka, and H. Tada, Appl. Phys. Express **17**, 097001 (2024).
23) Y. Hayashi, H. Shimada, and Y. Mizugaki, Jpn. J. Appl. Phys. **64**, 02SP42 (2025).
24) Y. Paquot, F. Duport, A. Smerieri, J. Dambre, B. Schrauwen, M. Haelterman, and S. Massar, Sci. Rep. **2**, 287 (2012).
25) H. Hasegawa, K. Kanno, and A. Uchida, Nanophotonics **12**, 869 (2023).
26) J. Nakayama, K. Kanno, and A. Uchida, Opt. Express **24**, 8679 (2016).
27) S. Kan, K. Nakajima, T. Asai, and M. Akai-Kasaya, Adv. Sci. **9**, 2104076 (2022).
28) R. Mito, K. Kanno, M. Naruse, and A. Uchida, Nonlinear Theory Appl., IEICE **13**, 123 (2022).
29) M. Akai-Kasaya, Y. Takeshima, S. Kan, K. Nakajima, T. Oya, and T. Asai, Neuromorphic Comput. Eng. **2**, 14003 (2022).
30) S. Kan, K. Nakajima, Y. Takeshima, T. Asai, Y. Kuwahara, and M. Akai-Kasaya, Phys. Rev. Appl. **15**, 24030 (2021).
31) K. Toprasertpong, E. Nako, Z. Wang, R. Nakane, M. Takenaka, and S. Takagi, Commun. Eng. **1**, 21 (2022).
32) Y. Usami et al., Adv. Mater. **33**, 2102688 (2021).
33) Y. Yamazaki and K. Kinoshita, Appl. Phys. Express **17**, 027001 (2024).
34) D. Sato et al., ACS Appl. Mater. Interfaces **15**, 49712 (2023).
35) N. Akashi, Y. Kuniyoshi, T. Jo, M. Nishida, R. Sakurai, Y. Wakao, and K. Nakajima, Adv. Sci. **11**, 2304402 (2024).
36) D. Nishioka, T. Tsuchiya, W. Namiki, M. Takayanagi, M. Imura, Y. Koide, T. Higuchi, and K. Terabe, Sci. Adv. **8**, eade1156 (2022).
37) T. Wada, D. Nishioka, W. Namiki, T. Tsuchiya, T. Higuchi, and K. Terabe, Adv. Intelligent Syst. **5**, 2300123 (2023).
38) K. Shibata, D. Nishioka, W. Namiki, T. Tsuchiya, T. Higuchi, and K. Terabe, Sci. Rep. **13**, 21060 (2023).
39) D. Nishioka, T. Tsuchiya, M. Imura, Y. Koide, T. Higuchi, and K. Terabe, Commun. Eng. **3**, 81 (2024).
40) Y. Yamaguchi, D. Nishioka, W. Namiki, T. Tsuchiya, M. Imura, Y. Koide, T. Higuchi, and K. Terabe, Appl. Phys. Express **17**, 024501 (2024).
41) T. Tsuchiya, D. Nishioka, W. Namiki, and K. Terabe, Adv. Electron. Mater. **10**, 2400625 (2024).
42) M. Takayanagi, D. Nishioka, T. Tsuchiya, M. Imura, Y. Koide, T. Higuchi, and K. Terabe, Mater. Today Adv. **18**, 100393 (2023).
43) D. Nishioka, Y. Shingaya, T. Tsuchiya, T. Higuchi, and K. Terabe, Sci. Adv. **10**, eadk6438 (2024).
44) D. Nishioka, T. Tsuchiya, T. Higuchi, and K. Terabe, Neuromorphic Comput. Eng. **3**, 034008 (2023).
45) W. Namiki, D. Nishioka, Y. Nomura, T. Tsuchiya, K. Yamamoto, and K. Terabe, Adv. Sci. **12**, 2411777 (2025).
46) W. Namiki, D. Nishioka, T. Tsuchiya, T. Higuchi, and K. Terabe, Nano Lett. **24**, 4383 (2024).
47) D. Nishioka, H. Kitano, W. Namiki, S. Souma, K. Terabe, and T. Tsuchiya, ACS Nano **19**, 36896 (2025).
48) L. Appeltant, M. C. Soriano, G. Van der Sande, J. Danckaert, S. Massar, J. Dambre, B. Schrauwen, C. R. Mirasso, and I. Fischer, Nat. Commun. **2**, 468 (2011).
49) D. Nishioka, K. Shibata, W. Namiki, K. Terabe, and T. Tsuchiya, Extended Abstracts of the 2025 Int. Conf. of Solid State Devices and Materials (SSDM 2025), 2025, p 189.
50) T. Kubota, H. Takahashi, and K. Nakajima, Phys. Rev. Res. **3**, 43135 (2021).
51) J. Dambre, D. Verstraeten, B. Schrauwen, and S. Massar, Sci. Rep. **2**, 514 (2012).
52) O. Srikimkaew, D. Banerjee, S. Azhari, Y. Usami, and H. Tanaka, ACS Appl. Electron. Mater. **6**, 688 (2024).
53) Y. Kubo, M. Yonezawa, H. Shima, Y. Naitoh, H. Akinaga, T. Nokami, T. Itoh, and K. Kinoshita, IEEE Access **12**, 153809 (2024).
54) E. J. Fuller, F. E. Gabaly, F. Léonard, S. Agarwal, S. J. Plimpton, R. B. Jacobs-Gedrim, C. D. James, M. J. Marinella, and A. A. Talin, Adv. Mater. **29**, 1604310 (2017).
55) D. Nishioka, T. Tsuchiya, T. Higuchi, and K. Terabe, Jpn. J. Appl. Phys. **59**, SIIG09 (2020).
56) W. Namiki, Y. Yamaguchi, D. Nishioka, T. Tsuchiya, and K. Terabe, Mater. Today Phys. **45**, 101465 (2024).
57) R. Nakane, A. Hirose, and G. Tanaka, Phys. Rev. Res. **3**, 033243 (2021).
58) R. Nakane, A. Hirose, and G. Tanaka, Phys. Rev. Appl. **19**, 034047 (2023).
59) G. Tanaka and R. Nakane, Sci. Rep. **12**, 9868 (2022).
60) D. Nishioka, T. Tsuchiya, W. Namiki, M. Takayanagi, K. Kawamura, T. Fujita, R. Yukawa, K. Horiba, H. Kumigashira, and T. Higuchi, Nanoscale Res. Lett. **15**, 42 (2020).
61) M. Takayanagi, T. Tsuchiya, D. Nishioka, M. Imura, Y. Koide, T. Higuchi, and K. Terabe, Mater. Today Phys. **31**, 101006 (2023).
62) D. Y. Kim, S. Miyoshi, T. Tsuchiya, and S. Yamaguchi, ECS Trans. **45**, 161 (2012).
63) T. Tsuchiya, M. Takayanagi, D. Nishioka, W. Namiki, and K. Terabe, J. Solid State Electrochem. **28**, 4367 (2024).
64) T. Tsuchiya, K. Terabe, and M. Aono, Appl. Phys. Lett. **105**, 183101 (2014).
65) T. Tsuchiya, M. Imura, Y. Koide, and K. Terabe, Sci. Rep. **7**, 10534 (2017).
66) M. Takayanagi, T. Tsuchiya, D. Nishioka, T. Higuchi, and K. Terabe, J. Mater. Chem. C **11**, 13311 (2023).
67) H. Kitano, D. Nishioka, K. Terabe, and T. Tsuchiya, Appl. Phys. Express **18**, 024501 (2025).
68) K. Terabe, T. Tsuchiya, T. Tsuruoka, H. Tanaka, I. Valov, J. K. Gimzewski, and T. Hasegawa, Solid State Ionics **430**, 116995 (2025).
69) W. Namiki, D. Nishioka, T. Tsuchiya, and K. Terabe, Neuromorphic Comput. Eng. **4**, 024015 (2024).
70) W. Namiki, T. Tsuchiya, D. Nishioka, T. Higuchi, and K. Terabe, Jpn. J. Appl. Phys. **63**, 03SP13 (2024).